A new view on orthogonal cutting model considering frictional dissipation

Fabio da Costa Figueiredo[a]* , Lavinia Maria Sanábio Alves Borges[a] , Jose Luis Lopes da Silveira[a] , Luísa de Amorim Makhoul Gomes[a]

[a]Mechanical Engineering Department, Federal University of Rio de Janeiro - UFRJ. Rio de Janeiro – RJ – Brazil. E-mails: fabiofigueiredo@mecanica.ufrj.br, lavinia@mecanica.ufrj.br, jluis@mecanica.ufrj.br, luisa.makhoul@mecanica.coppe.ufrj.br

* Corresponding author

https://doi.org/10.1590/1679-78258208

Abstract

This study aims to refine orthogonal cutting analysis using numerical methodology of limit analysis, focusing on predicting cutting forces and contact stresses more accurately. Unlike prior models, it incorporates frictional dissipation and considers sticking or sliding as part of the solution. It is shown that shear stress in sticking contact cannot be equated to shear yield stress, as typically imposed, leading to stress overestimation. The workpiece is treated as a deformable body, discretized with finite elements, while the tool is rigid. Interaction between them follows contact conditions in normal and tangential directions. Inputs include cutting conditions, friction coefficient, and material properties. Results encompass cutting forces, velocity and stress fields, and shear regions. Discrepancy between the shear angle predicted by Merchant and those ones obtained numerically is discussed. Finally, results are compared with experimental data found in literature. This approach provides a more accurate cutting model for determining cutting forces and contact stresses, which is crucial for estimating tool wear and life.

Keywords

Orthogonal cutting, Finite elements, Limit analysis, Frictional interface.

Graphical Abstract
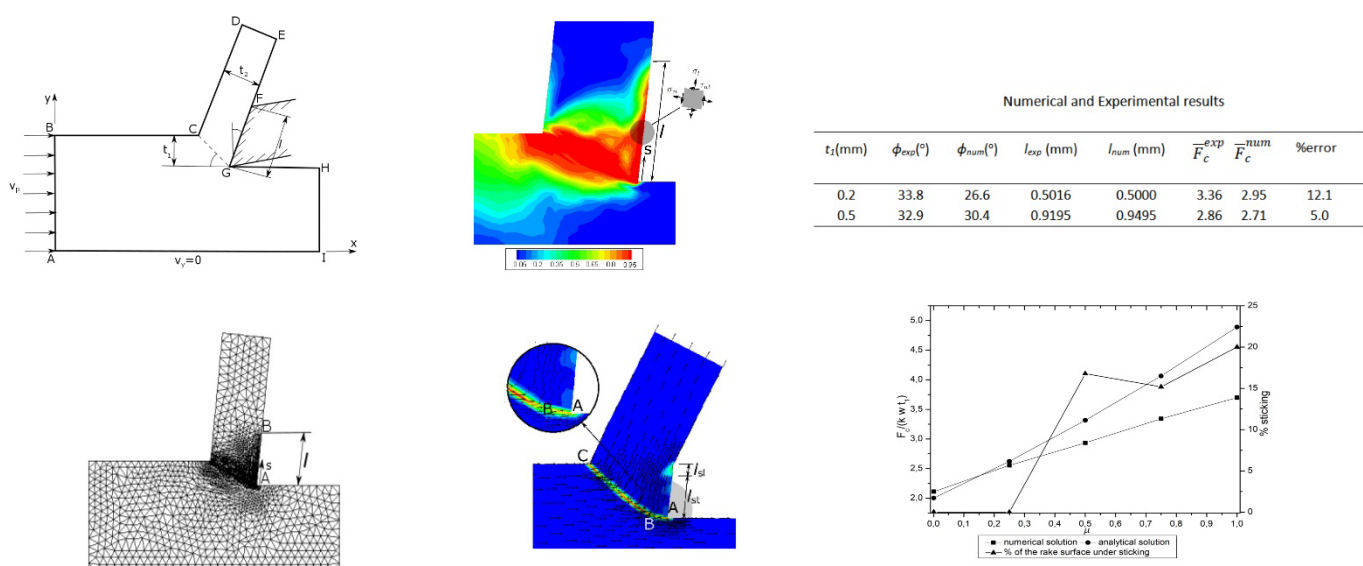
1 INTRODUCTION

Machining is a manufacturing operation in which a sharp tool is used to cut a workpiece in order to obtain a piece with a required geometry. This operation involves shear deformation of the workpiece to form a chip and a new surface, according to Groover (2010). The study of machining process is important for evaluation of energy consumption, tool life and wear, surface integrity and surface finishing. As in Strenkowski and Moon (1990), in the cutting processes, high stresses and temperatures are involved and it can lead to premature wear or even failure of the tool. The cutting process is conventionally divided into two general cases, termed orthogonal and oblique cutting. In orthogonal cutting, the cutting speed and the cutting edge are orthogonal, while in oblique cutting this orthogonality does not occur, as in Groover (2010). In this work, the focus will be on the analysis of orthogonal cutting, which can be represented by a two-dimensional problem.

Despite being a simple process, orthogonal cutting is of interest due to its two-dimensional modeling. Due to this, methodologies are being proposed to model oblique cutting processes such as milling, which are inherently three-dimensional, as a planar equivalent orthogonal cutting problem, as observed in Wu et al. (2023) and Cai et al. (2024). The orthogonal cutting model has also been used in investigating the influence of cutting edge geometry to assess process forces and surface integrity in carbon fiber reinforced plastics, like in Peter et al. (2022), Sauer et al. (2019). Furthermore, the orthogonal cutting model has gained interest in micro-machining modeling, a process used for manufacturing medical, aerospace, and micro-components for the electronics industry. However, modeling the process at the microscale is more complex than at the macroscale due to scale effects and dependence on crystallographic orientations of the crystal grains, as observed in Medina-Clavijo et al. (2021). At microscale, the uncut chip thickness and the tool edge radius are comparable in size and plowing action becomes more relevant than shearing, according to Afsharhanaei et al. (2016). The chip formation is also influenced by micropores, material fractures, inclusions, grain boundaries, and dislocation interactions, pursuant to Wojciechowski et al. (2019).

Hence, acquiring a deeper insight into the phenomenology of the cutting process, the mechanisms involved in chip formation, and the interaction between the chip and the tool has the potential to drive the advancement and refinement of models, thereby enhancing their predictive capacity. There are four methods to predict cutting forces: theoretical (analytical), experimental, finite element (FEM) simulation and mechanistic modeling, as seen in Zhou and Ren (2020). A purely experimental analysis is expensive and so time consuming while theoretical and mechanistic modeling only few variables of interest like cutting forces are evaluated. In this context, the use of finite element analysis is advantageous because it allows the acquisition of both global quantities such as cutting forces and local quantities such as contact stresses and the determination of sliding/sticking regimes at chip-tool interface. Considering the high stresses developed within both the workpiece and at the chip-tool contact, along with the significant rates of deformation inherent in the cutting process, plasticity theory should be incorporated into both analytical and numerical methods.

The analysis of the cutting process is strongly influenced by the contact conditions between the chip and the tool. In this contact region, sticking commonly occurs near the cutting edge, while sliding occurs at other points until the chip-tool separation point. As found in Grzesik (2017), this two-zone model proposed by Zorev, the normal stress gradually decreases from its maximum at the cutting edge until it becomes null at the chip-tool separation point, while the tangential stress remains constant in the sticking region, equal to the shear yield stress, and is proportional to the normal stress in the sliding region, according to the Coulomb friction model. In the development of some analytical solutions, it is assumed an exponential function to describe the nor- mal stress distribution along the rake face, as observed in Zhang et al. (2017) and Ozlu et al. (2010). This premise has also been implemented in finite element codes, such as in Molinari et al. (2011), Denguir et al. (2017), and Santos et al. (2023). In Santos et al. (2023), the portion of the contact region under sticking is assumed beforehand to be the thickness of the undeformed chip.

The aim of this work is to analyze the orthogonal cutting process using the limit analysis methodology, considering the frictional dissipation term according to the formulation proposed in Figueiredo and Borges (2017, 2020). Dissimilar to incremental analysis, which computes intermediate steps and data until occurrence of plastic collapse, as in Lubliner (1990), limit analysis is a direct method and the plastic collapse is determined from the solution of an optimization problem.

In this approach, a unitary velocity field is imposed to the workpiece as a non-homogeneous boundary condition while the tool is considered as a stationary rigid body. Based on work of Borges et al. (1996), the limit analysis problem is solved iteratively and besides the plastic collapse power calculation (in this application, compared to the cutting forces), it aims the determination of the plastically admissible stress field, the plastic strain rate field that is kinematically compatible to the velocity field and the plastic multiplier, associated with determination plastic dissipation and related to the determination of shear zones in the cutting process.

Some solutions using direct methods, whether analytical or numerical, assume prior behaviors in the contact region or in the primary shear region. The Merchant model assumes the primary shear region to be thin, that stresses in this region are

uniform, and that there is sliding in the chip-tool contact, according to Kalpakjian and Schmid (2016). As found in Armarego and Brown (1969), Oxley thin-shear-zone analysis has applied a simplified slip-line field to model metal cutting. Normal and shear stresses at tool-chip contact are assumed as a uniform distribution. Later, non-uniform stresses distribution was assumed. In Kudo (1965), slip-lines fields were proposed for restricted and unrestricted cutting tool faces by considering sticking friction. Also, Lee and Shaffer determined an expression for the shear angle by analyzing the stress state of the material in the plastic state and taking into account the directions of the slip lines in the chip, according to Kovrizhnykh (2009).

A contribution of this work is the consideration of friction at the chip-tool interface by including the friction dissipation term in the limit analysis formulation. As a solution to this problem, the tangential velocities at the contact are calculated, as well as the contact stress field. This approach has implications in the analysis of the orthogonal cutting process because, unlike the commonly adopted models previously cited and based on the Zorev model, in this proposed model: (i) the determination of the regions of sticking and sliding at the contact occurs naturally through the solution of the contact problem; (ii) in the occurrence of adhesion, the tangential contact stress (shear) behaves as a reaction to the zero tangential velocities obtained from the solution of the contact problem. This stress component does not reach the material's shear yield because plastic admissibility is verified and depends on the normal stress components, not on a pure shear stress state. On the other hand, imposing the tangential component as the shear yield can lead to an overestimation of the stress state at contact.

This numerical approach also enables the determination of primary, secondary, and tertiary shear regions in the cutting process through an adaptive mesh technique. This technique is capable of capturing discontinuities that arise from localized plastic deformations during plastic collapse. It is described in Borges et al. (2001), and through a posteriori indicator, it facilitates the localization of slip bands in the mesh, considering mesh refinement and redefinition of the oriented element stretching. At each step, the slip lines become more defined, and a convergence of collapse power is observed.

The procedure for analyzing orthogonal cutting using the proposed limit analysis methodology involves the need for a steady-state configuration. As an initial configuration, the Merchant model is taken as a reference, and the dimensions of the deformed body are taken in relation to its primary shear angle, obtained from the minimization of cutting energy, as in Groover (2010), Grzesik (2008). However, in Molinari and Moufki (2008), it is shown that there is a discrepancy between the primary shear angles predicted by Merchant and those obtained by numerical simulation and experimental measurements. In addition to the influence of material work hardening and softening due to temperature effects, Molinari and Moufki (2008) points out that the Merchant model does not take into account the sensitivity of the results to the geometry of the free surface and it is based on a configuration without chip formation. After chip formation, the primary shear angle may be greater or less than theoretically predicted, and the analytical cutting force may be underestimated. In this context, the shear angle used in the initial configuration of the numerical model is measured at the end of the simulation, thus obtaining the optimal primary shear angle, and from this new angle, the steady-state configuration of the body is updated.

The presented analyses consist of two parts. In the validation stage, the numerical solution is compared with the experimental results from Abouridouane et al. (2015). The experiment was carried out on a vertical broaching machine, and the entire process was captured by a high-speed camera. Experimental contact lengths were measured from the images provided by the author, and from force graphs, ten points were extracted and averaged to obtain the cutting and feed forces of the process. The numerical results were compared with these data. Furthermore, the stress state in the contact region and the coexistence of plasticization in contact with either sticking or sliding regimes are discussed.

In the subsequent stage, a more comprehensive analysis was conducted to discuss the relationship between numerical and analytical cutting forces with the occurrence of sticking in an unrestricted contact tool considering the rake angles $\alpha = 0^\circ$ and $\alpha = 6^\circ$. Then, the contact region length was fixed (restricted or controlled contact tool) and by varying the friction coefficient at the interface, it is shown that the cutting forces tend towards an asymptotic value and become independent of the friction coefficient as sticking regions increase. Finally, it is shown that the optimal primary shear angles predicted in Molinari and Moufki (2008) are confirmed. The optimal angles obtained numerically and those ones predicted by Merchant approach each other only when there is no friction in the chip-tool contact. In this case, the contact length is on the order of the undeformed chip thickness.

2 METHODOLOGY

2.1 Geometrical model

The workpiece is modelled as a deformable body under 2-D plane strain hypothesis, considering an elastic perfectly-plastic material under von Mises criterion. This specimen is discretized into finite elements while the tool is treated as a

stationary rigid body. The cutting tool is not represented in the numerical simulation and its interaction with the workpiece is imposed by contact conditions.
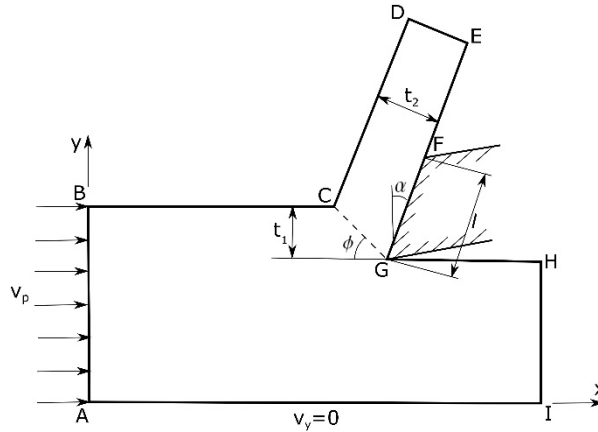

Figure 1 Geometry and dimensions of the workpiece.

Figure 1 depicts the cutting parameters and the geometry of the workpiece. A unitary velocity field v_p is imposed on the boundary AB, while the tool, with a contact length l, is considered fixed. The boundary AI allows for horizontal movement, t_1 and t_2 represent the thicknesses of the undeformed and deformed chip, respectively, ϕ is the primary shear angle, and α is the tool's rake angle.

As an initial guess, the primary shear angle ϕ is determined according to Merchant's model, found in Groover (2010), Grzesik (2008):

$$\phi_M = \frac{\Pi}{4} + \frac{1}{2}(\alpha - \beta) \tag{1}$$

where: ϕ_M is the primary shear angle predicted by Merchant, and β is the friction angle, such: $\beta = atan(\mu)$ and μ is the friction coefficient.

From primary shear angle ϕ, the chip thickness t_2 is calculated geometrically from Figure 1:

$$t_2 = t_1 cos(\phi - \alpha)/sin(\phi) \tag{2}$$

The minimum contact length l is set *as $l = t_1/cos(\alpha)$*, considering a restricted contact tool. If the distribution of normal stresses satisfies the condition $\sigma_n < 0$ along the entire contact length l, the tool is considered to be in restricted contact. By incrementally increasing the contact length, the chip- tool separation point can be identified when the normal stress σ_n approaches zero at point F in Figure 1. Subsequently, an unrestricted contact tool is obtained.

In Figure 1, the chip-tool interaction is imposed through contact conditions: permanent contact between chip-tool is assumed (there is no normal gap and no normal relative velocity) and in the tangential direction, the tangential velocities and reaction stresses at the contact are determined by solving a complementarity problem.

In the numerical model, the continuum media is discretized into finite elements and the limit analysis problem is solved. From the solution of the limit analysis problem, the velocity and stress fields are determined, as well as the zones of plastic dissipation, associated with the shear regions in the cutting process.

In the establishment of the steady-state configuration, the determination of the primary shear angle holds significant importance. However, as demonstrated in Molinari and Moufki (2008), the shear angle predicted by Merchant may not be the most representative, as it was deduced without considering chip formation. The referred work infers that the primary shear angle may be greater or less than that estimated by Merchant after chip formation, defining an optimal shear angle ϕ^*. As a consequence, if $\phi^* \geq \phi_M$, ϕ_M minimizes the cutting force $F_c(\phi)$. Otherwise, $\phi = \phi^*$ minimizes $F_c(\phi)$ and $F_c(\phi^*) > F_c(\phi_M)$.

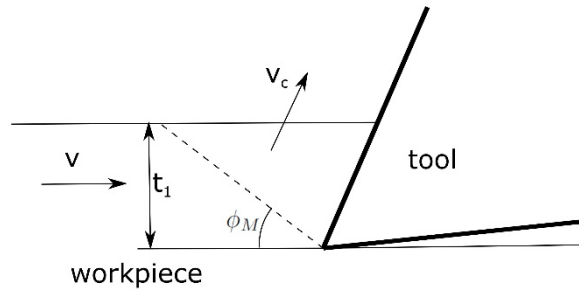The figures below represent these two situations:
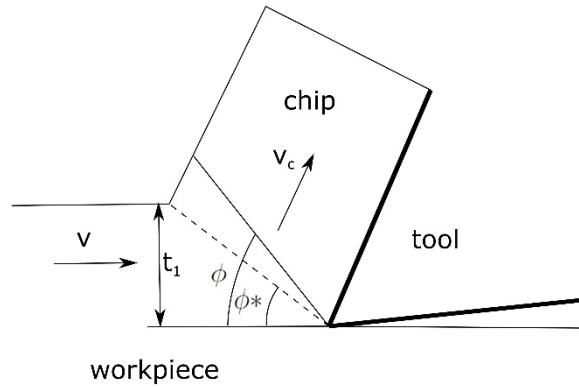
Figure 2 Workpiece with an initial flat surface.

Figure 3 Workpiece after chip formation. The shear angle φ = φ$_M$, if φ* ≥ φ$_M$ and φ = φ*, if φ* ≤ φ$_M$.

Figures 2 and 3 illustrate the distinction between the shear angles ϕ_M and ϕ^*. When considering chip formation, Molinari and Moufki (2008) formulates the subsequent expressions for computing analytical cutting forces:

$$\frac{F_c}{kt_1 w} = \frac{cos(\beta)}{sin(\phi)cos(\phi+\beta)}, \phi \leq \phi^* \tag{3}$$

$$\frac{F_c}{kt_1 w} = \frac{cos(\beta)}{tan(\phi^*)cos(\phi)cos(\phi+\beta)}, \phi \geq \phi^* \tag{4}$$

Examining the behavior of the expressions provided in Equations (3) and (4) with the angle ϕ, it becomes evident that depending on the relationship between ϕ^* and ϕ_M, the cutting forces estimated by Merchant may be underestimated. In this study, the optimal angle ϕ^* is determined numerically, and these expressions serve for comparing with the obtained numerical cutting forces and for establishing the conditions under which these expressions hold validity.

It is worth noting that the theoretical Merchant angle, used as a reference for determining the initial geometry of the steady-state configuration in this work, not only neglects chip formation but also assumes sliding throughout the entire contact region between the chip and the tool. The following figure illustrates the steps to obtain the steady-state configuration:
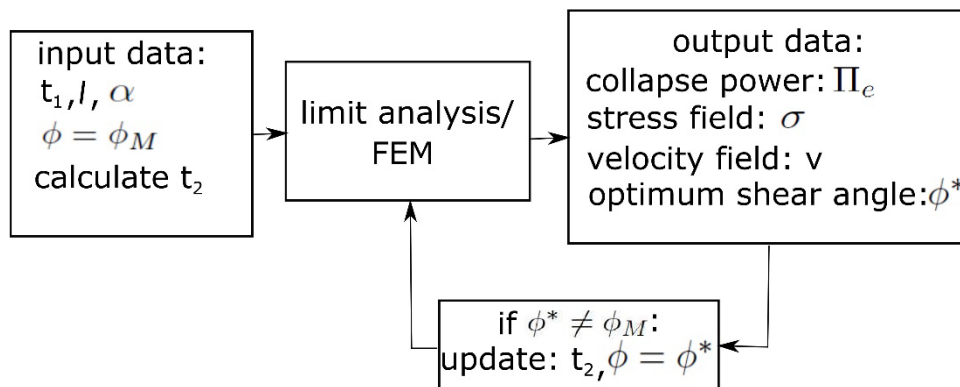

Figure 4 Stages of constructing the steady-state configuration.

As seen in Figure 4, the cutting parameters t_1, l, α are selected, and initially setting $\phi = \phi_M$, t_2 is calculated. The workpiece is discretized using finite elements and from the solution of the limit analysis problem, the optimal shear angle ϕ^* is obtained, and the geometry is updated.

Moreover, in some cases the steady-state configuration *does* not match the chip flow velocity field. Then, based on the proposal by Tyan and Yang (1992), which suggests the use of a stream angle η to characterize chip geometry under steady-state conditions, this study introduces the stream angles, η_1 and η_2, aiming to achieve a more accurate alignment between the chip geometry and velocity fields, as illustrated in the Figure 5 below:
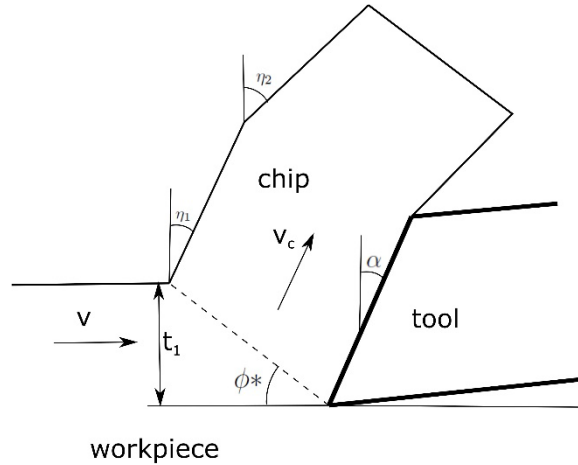

Figure 5 Adaptive chip configuration with two angles.

These two angles are employed to capture the velocity field behavior of the material flowing over the rake surface, represented by η_1, and the behavior of the velocity field after losing contact with the tool, depicted by η_2. Both angles are determined so that the velocity vectors are tangent to the chip geometry contour.

2.2 Limit Analysis Formulation

According to Chen and Liu (1990), Lubliner (1990), limit analysis is a direct method which aims the determination of an external collapse power that results in the incipient plastic flow under a permanent regime configuration. It consists in finding a collapse power Π_e, a plastic admissible stress field $\boldsymbol{\sigma}$, associated with the plastic strain rate $\boldsymbol{d^p}$, compatible to the kinematically admissible velocity field $\boldsymbol{v}$.

In this formulation, it is assumed that the contact region is known and that the deformable and rigid bodies remain in contact in the steady-state condition. Separation is not admissible. This condition is described by restrictions at normal direction: normal gap ($g_n = 0$), as in Chabrand et al. (1998), Wriggers (1999), and normal relative velocities (w_n) is also zero. The Signorini conditions at the normal direction are posed as follows:

$$w_n = 0, r_n < 0, r_n w_n = 0 \tag{5}$$

where: w_n is the normal relative velocity and r_n is the normal force.

At the tangential direction, denoting the Coulomb friction function as $\mathcal{F}(\boldsymbol{r_t}, r_n)$ as in Michalowski and Mroz (1978), Raous (1999), Saxcé and Bousshine (1998), the following applies:

$$\mathcal{F}(r_t, r_n) = ||\boldsymbol{r}_t|| + \mu r_n \leq 0 \tag{6}$$

where: μ is the friction coefficient, $\mathbf{r}_t$ is the tangential force and $r_n < 0$ represents the occurrence of contact.

The Coulomb friction law describes the occurrence of sliding or sticking regimes:

$$\text{If } \mathcal{F}(\mathbf{r}_t, r_n) = 0, \text{ then } \mathbf{w}_t = -\xi \frac{\partial \mathcal{F}(\mathbf{r}_t, r_n)}{\partial r_t} \text{ (sliding)} \tag{7}$$

$$\text{else: } \mathrm{w}_t = 0 \text{ (sticking)} \tag{8}$$

$$\mathcal{F}(\mathbf{r}_t, r_n)w_t = 0 \text{ (complementarity relation)} \tag{9}$$

where: $\xi \geq 0$ is a proportionally constant and Equation (9) expresses a complementarity relation between $\mathcal{F}(r_t, r_n)$ and w_t.

Once assuming the hypothesis of permanent contact, necessary to ensure the process under steady-state conditions, the normality law as shown in Equation (7) applies locally, as the normal reaction forces are known and determined through equilibrium conditions, pursuant to Michalowski and Mroz (1978), Nguyen (2000). This allows for the deduction of the static, kinematic, and mixed principles of limit analysis with contact and friction conditions, presented in detail in Figueiredo and Borges (2020).

2.3 Computational Procedure

For the solution of the limit analysis problem, the continuum domain is discretized into triangular elements, with linear interpolation for the stress field and quadratic interpolation for the velocity field. Regarding notation, the fields to be presented hereafter are referred as discrete variables. Considering **B** as the discrete strain operator, relating the strain rates **d**^{p} and the velocity field **v**, the discrete form of the mixed limit analysis formulation is posed as follows:

$$\Pi_e = \min_{\mathbf{v}, \mathbf{w}_t} \max_{\sigma, \mathbf{r}_t}(\sigma \cdot \mathbf{B}\mathbf{v} - \mathbf{r}_t \cdot \mathbf{w}_t) \tag{10}$$

such that:

$$\boldsymbol{f}(\sigma) \leq \mathbf{0} \text{ in } \mathcal{B} \tag{11}$$

$$\mathcal{F}(\mathbf{r}_t, r_n) \leq \mathbf{0} \text{ at } \Gamma_c \tag{12}$$

$$\mathbf{w}_n = \mathbf{0} \text{ at } \Gamma_c \tag{13}$$

where: r_n and $\boldsymbol{r_t}$ are respectively, normal and tangential reaction forces at contact boundary Γ_c, $\boldsymbol{f}(\sigma)$ is the yield function and $\mathcal{F}(r_t, r_n)$ is the Coulomb friction function.

The computational procedure described in Figueiredo and Borges (2020) consists in solving the set of optimum conditions equations obtained from the optimization problem (10) with the constraints (11)-(13). This set of equations is solved iteratively by a quasi-Newton algorithm.

A condensation technique is applied to formulate and solve the linear complementarity problem (LCP) in contact, whose solution consists in finding the reaction forces r_n, $\boldsymbol{r_t}$ and relative tangential velocities $\boldsymbol{w_t}$ at the contact. Then, the field of free velocities (outside of contact) is determined.

In the analysis of the orthogonal cutting process, the workpiece is discretized into triangular elements. Applying the mesh adaptation technique from Borges et al. (2001), the figure below shows a finite element mesh obtained:
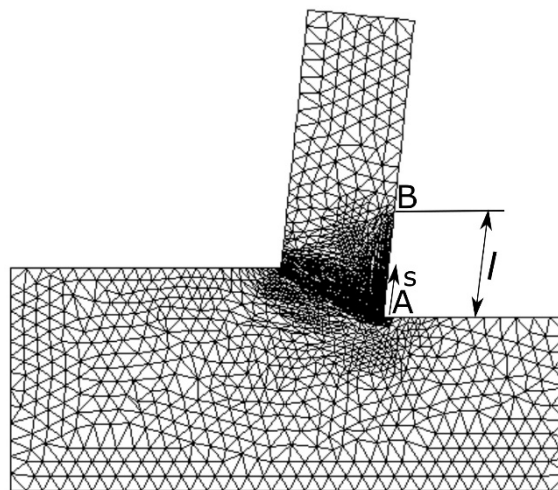

Figure 6 Adaptive mesh for the workpiece. Contact conditions are applied in the contact region A-B, with length l.

The adaptive mesh shown in Figure 6 is obtained gradually by solving the limit analysis problem successively. It is observed that adaptation occurred in the primary and secondary shear regions. This procedure is carried out within the limit analysis/FEM block of Figure 4. Once the mesh converges, the optimal shear angle ϕ^* is measured, and the steady-state configuration is updated if necessary.

3 RESULTS

This section consists of two parts: an initial step involving a comparison with experimental results found in Abouridouane et al. (2015). Following this, a broader analysis is conducted, allowing for the examination of the influence of parameters such as friction coefficient, occurrence of adhesion and sliding regions, and tool rake angles on estimating the contact region, assessing cutting forces, and primary shear angles. The theoretically predicted optimal shear angles, as presented in Molinari and Moufki (2008), were numerically determined and applied to equations (3) and (4) to compute the analytical cutting forces, which will be compared with the numerical cutting forces.

3.1 Validation

In this section, the experimental results carried out in Abouridouane et al. (2015) are briefly presented hereafter and they will be compared to the numerical results obtained from the limit analysis methodology presented in this paper. The experiment was carried out on a vertical broaching machine tool and in order to capture the complexity of the cutting operation, a high-speed camera was coupled allowing high-speed filming and thermography. The cutting tool was mounted on a three-component piezoelectric platform from Kistler. The tool is fixed and the chip formation was recorded with Vision Research Phantom v7.3 camera. Schematically, one may observe the experimental device (Figure 7):
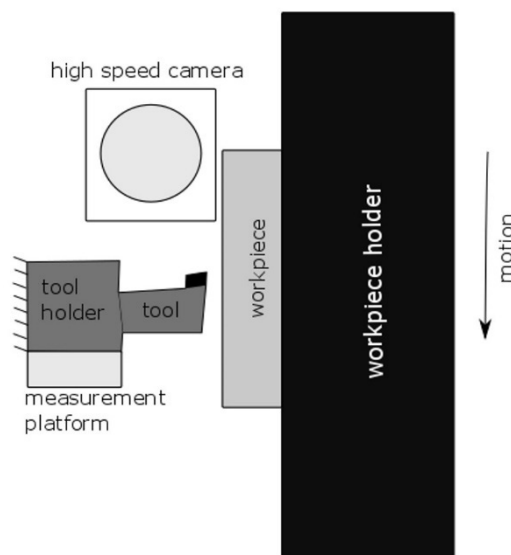

Figure 7 Experimental setup (schematically): the tool is fixed and the workpiece executes a translational motion.

The workpiece is a normalized carbon steel AISI 1045, with dimensions 3.5 mm x 40 mm x 200 mm. Tool: Sandivik H13A, rake angle α = 6º, a sharp tip with r < 5 μm. The author presents experimental results concerning v_c=150 m/min and uncut chip thickness t_1 varies from 0.04 mm to 0.50 mm. The cutting width is w = 3.5 mm. From Figures 2 and 9 A from the referenced paper, the chip-tool contact lengths l_{exp} and the primary shear angle ϕ_{exp} were measured by the software Image J, regarding t_1=0.2 mm and t_1=0.5 mm. The cutting and feed forces F_c^{exp} and F_f^{exp} were measured from the graphs provided by Abouridouane et al. (2015). Disregarding the instants related to the transient regime, these forces were determined as an average of ten points under steady-state regime. To generalize the results, the cutting forces were dimensionless by the cutting thickness w, the undeformed chip thickness t_1, and the shear yield stress of the material k.

Given the experimental forces F_c^{exp} and F_f^{exp}, the primary shear angle ϕ_{exp}, and the cutting parameters t_1 and w, the shear yield stress k is calculated, according to DeVries (1992):

$$k = \frac{F_c^{exp}\sin(\phi)\cos(\phi) - F_f^{exp}\sin^2(\phi)}{t_1 w} \qquad (14)$$

The experimental results are summarized in the table below:

Table 1 Experimental results

t_1(mm)	ϕ_{exp}(°)	l_{exp} (mm)	μ	F_c^{exp} (N)	F_f^{exp} (N)	k(MPa)	$\overline{F}_c$
0.2	33.8	0.5016	0.6797	1447.1	793.6	634.6	3.36
0.5	32.9	0.9195	0.4809	3222.0	1160.8	643.9	2.86

where: $\overline{F}_c$ is the non-dimensional cutting force, defined by $\overline{F}_c = F_c/(t_1 wk)$.

In the numerical model, the parameters t_1, α, and the friction coefficients μ from Table 1 were used to initially determine the shear angle through Equation (14) and to compute the chip thickness t_2 using Equation (2). In constructing the geometric model, the contact length between chip-tool is not known in advance. To determine it, a parametric study was conducted by varying the contact length and observing the distribution of normal contact stresses, whereby the contact length is numerically determined when the normal stress approaches zero at the chip-tool separation point.

Hence, the numerical contact lengths were determined for both cases as outlined in Table 1, based on the stress distributions in the contact region, as depicted in the subsequent figures. The coordinate s originates from position A (cutting edge) as depicted in Figure 6, extending up to point B, representing the separation point, with $0 \leq s/l \leq 1$.
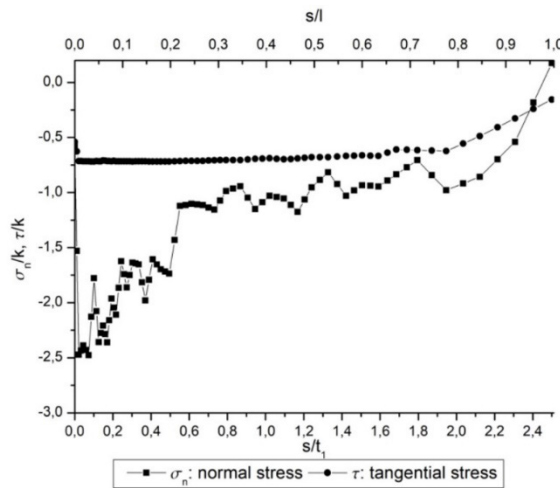

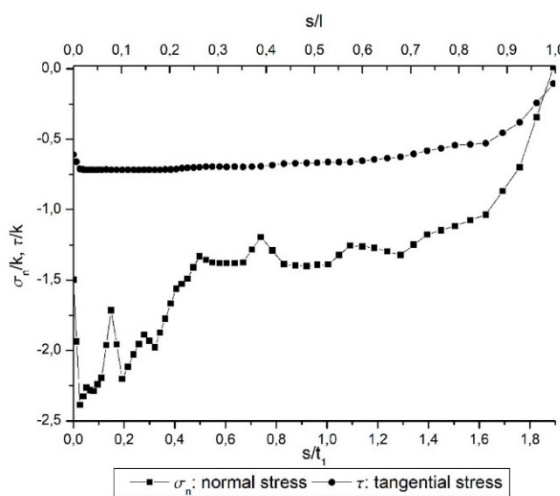**Figure 8** Contact stresses for t_1=0.2 mm.

Figure 9 Contact stresses for t_1=0.5 mm.

In Figures 8 and 9, the contact stresses were parameterized by the shear yield stress k. It is observed that the normal stress approaches zero at the separation point, while the tangential stress remains constant in part of the contact region

until it decreases in the vicinity of the coordinates s/l = 0.8 and s/l = 0.85. The following table provides a comparison between experimental and numerical results:

Table 2 Numerical and Experimental results

t_1(mm)	ϕ_{exp}(°)	ϕ_{num}(°)	l_{exp} (mm)	l_{num} (mm)	$\overline{F}_c^{exp}$	$\overline{F}_c^{num}$	%error
0.2	33.8	26.6	0.5016	0.5000	3.36	2.95	12.1
0.5	32.9	30.4	0.9195	0.9495	2.86	2.71	5.0

In Table 2, the numerical and experimental shear angles, contact lengths, and dimensionless cutting forces are compared. Regarding the shear angle ϕ_{num}, it was obtained following the procedure outlined in Figure 4. The initial values were 30.9° and 35.1°, respectively. The optimal angles ϕ^* obtained are the ϕ_{num} angles from the aforementioned table. The following figures depict the initial shear angles ϕ_M, estimated by the Merchant model in Equation (14), and the optimal angle ϕ^* obtained:
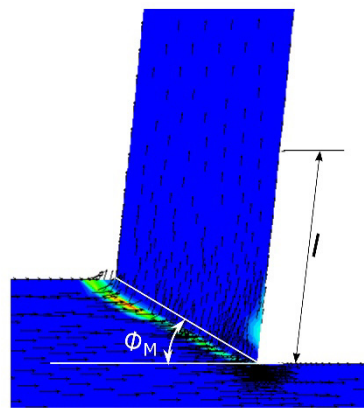

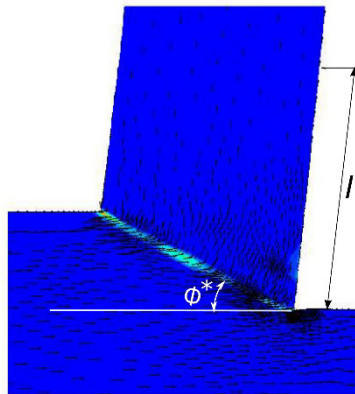**Figure 10** Shear angle predicted by Merchant model for t_1=0.2 mm.

Figure 11 Optimum primary shear angle.

Figure 10 illustrates that the angle predicted by Merchant, ϕ_M does not adequately describe the steady-state configuration. In contrast, the shear angle ϕ^* in Figure 11 corresponds to the steady-state configuration obtained from the limit analysis solution.

Regarding the contact lengths in Table 2, it is observed that there is good agreement between the experimentally measured lengths l$_{exp}$ and those obtained numerically l$_{num}$. As for the cutting forces, there is a difference of 12.5% and 5.0% for the cases t_1 = 0.2 mm and t_1 = 0.5 mm, respectively.

Through the limit analysis methodology, one can determine the regions of the workpiece where plasticization has occurred, indicated by the von Mises equivalent stress σ$_{eq}$ reaching the shear yield stress k.
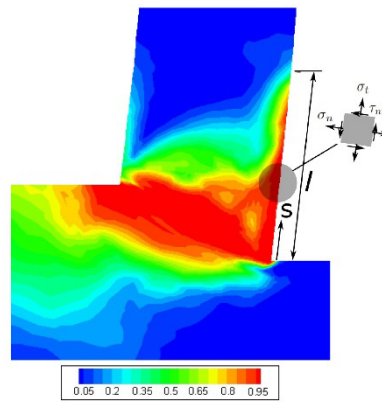
Figure 12 Mises equivalent stress σ_{eq} /k for t_1=0.2 mm (l/t1 = 2.5).
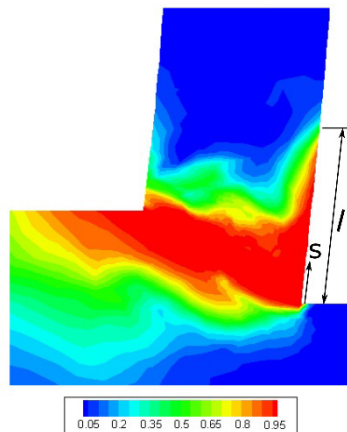

Figure 13 Mises equivalent stress σ_{eq} /k for t_1 = 0.5 mm (l/t$_1$ = 1.839).

In Figures 12 and 13, it is evident that plasticization predominantly occurs within the contact region *l* as the ratio σ_{eq}/k approaches 1. Through this methodology, by simultaneously verifying the inequalities regarding stress admissibility (as represented by the constraint in Equation (11)) and the contact conditions (expressed by the constraint in Equation (12)), regions of sticking and sliding can occur while simultaneously experiencing plasticization at contact points. Unlike traditional approaches, where in the case of sticking, the condition is directly imposed on the shear component as τ_{nt} = k, the equivalent stress depends on the normal stress components σ_n and σ_t, as well as the shear component τ_{nt}, as emphasized in the detail in Figure 12.

The regions of sticking and sliding can be determined through the velocity field, which is the solution to the limit analysis problem stated in (10)-(13):
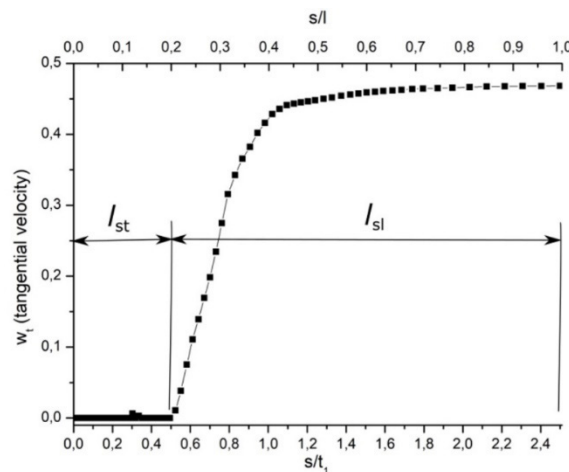

Figure 14 Tangential velocity at the chip- tool contact for the *case t_1 = 0.2 mm. l/ t_1 = 2.5, 0 ≤ s ≤ l.*
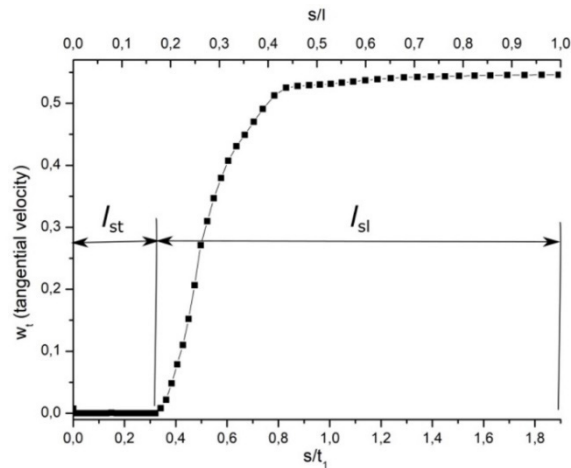
Figure 15 Tangential velocity at the chip- tool contact for the case $t_1 = 0.5$ mm. $l/t_1 = 1.839$, $0 \leq s \leq l$.

From the distribution of tangential velocities depicted in Figures 14 and 15, the contact lengths under sticking, denoted as l_{st}, and under sliding, denoted as l_{sl}, are observed. The sticking regions ($w_t = 0$) correspond to $l_{st}/l = 19\%$ and $l_{st}/l = 17\%$ of the contact length, respectively, while sliding occurs beyond these points. These findings align with the complementary relationship established in equation (9): in the case of sticking, $w_t = 0$ and $|\tau| + \sigma_n < 0$. Conversely, during sliding, $w_t > 0$ or $w_t < 0$ and $|\tau| + \sigma_n = 0$. Referring back to Figures 12 and 13, due to the high stresses, points in contact reach plasticization, regardless of whether sticking or slipping occurs.

From the distributions of shear and normal stresses, it becomes feasible to estimate an average friction coefficient within these two regions. During sliding, it is expected that the ratio between shear and normal stresses ($\mu_{sliding}$) will converge towards the applied friction coefficient μ, while in the sticking region, an apparent friction coefficient $\mu_{sticking}$, dissimilar to μ, is expected:

Table 3 Apparent friction coefficient

t_1(mm)	μ	$\mu_{sticking}$	$\mu_{sliding}$
0.2	0.6797	0.3686	0.6725
0.5	0.4809	0.3459	0.4970

In Table 3, in the case of sticking, $\mu_{sticking} < \mu$, and in the sliding region, $\mu_{sliding}$ approaches μ. In the latter case, this slight difference is observed since the contact stresses are not directly imposed as a boundary condition. In the case of sticking, chip material flows over the adhered material onto the rake face. Due to sticking, the formation of the secondary shear zone is observed, as depicted in the following figures:
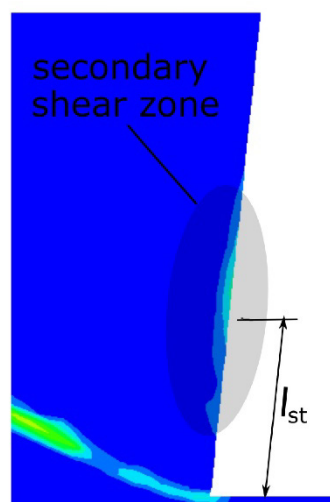

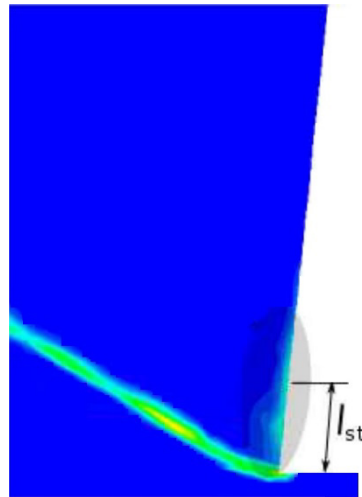**Figure 16** Secondary shear zone for the case t1 = 0.2 mm.

Figure 17 Secondary shear zone for the case t1 = 0.5 mm.

In Figure 16, the secondary shear occurs in the final region of the contact under sticking. In Figure 17, the secondary shear begins at the cutting edge position and extends through the sticking region. The primary and secondary shear regions are related to the equivalent rate of plastic deformation developed, while Figures 12 and 13 are related to the stress state. In terms of stresses, plasticization occurs over a more extensive region of the workpiece. However, at these points, zero deformation rates may be observed.

3.2 Analysis of Orthogonal Cutting

In this section, a comprehensive study will be conducted using the presented limit analysis formulation. The behavior of cutting forces and their correlation with the friction coefficient at the interface, the development of regions in sticking and sliding, and the rake surface angle will be addressed. These analyses will follow the same procedure as before, involving the evaluation of the optimal shear angle and determining the contact length by checking the condition of the normal stress σ_n at the separation point between the chip and the tool, as it approaches zero. Evaluating this condition, the contact lengths l/t_1 are determined as a function of the friction coefficients and exhibit dependency on the rake angles, evaluated for $\alpha = 0^o$ and $\alpha = 6^o$:
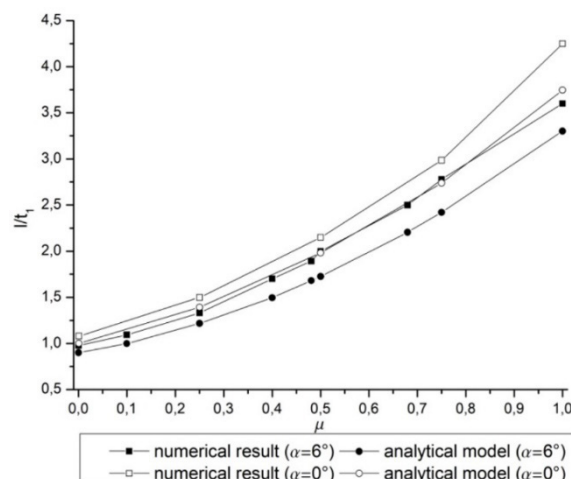

Figure 18 Contact lengths x friction coefficient.

In Figure 18, to assess the coherence of the results, the numerical results were compared with some expressions found in Fatima and Mativenga (2013). There are several models for determining the contact length, based on analytical, statistical, empirical, and dimensional analysis methods. Among the various models tested, the analytical models of Hahn, Rubenstein, and Zorev presented expressions that best approximate the numerical results obtained. The expression derived by Zorev is presented as follows (Fatima and Mativenga (2013)):

$$l = mt_2(tan\beta + tan(\phi - \alpha))$$ (15)

where: α, ϕ and β are, respectively, the rake, primary shear and friction angles, t_2 is the deformed chip thickness and m is a material constant.

While some models for predicting the contact length are calculated considering only the undeformed chip thickness t_1 or chip thickness t_2, and cutting speed, the models by Hahn, Rubenstein, and Zorev consider, in addition to t_1 or t_2, parameters such as the tool rake angle α, primary shear angle ϕ, and friction angle β. Assuming m as unitary in Equation (15), it is observed that the numerical and analytical solutions in Figure 18 are proportional. Differing by a factor of around 1.10, Equation (15) accurately describes the numerical results obtained.

After determining the contact lengths, the behaviors of the cutting forces are evaluated, taking into account the rake angles of 0o and 6o, as well as the friction coefficient and the occurrence of sticking at the chip-tool interface.
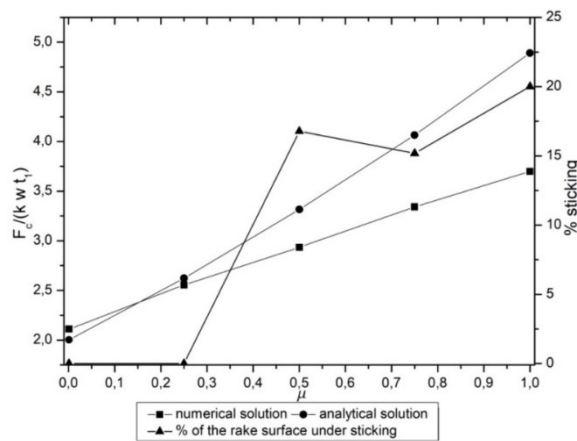

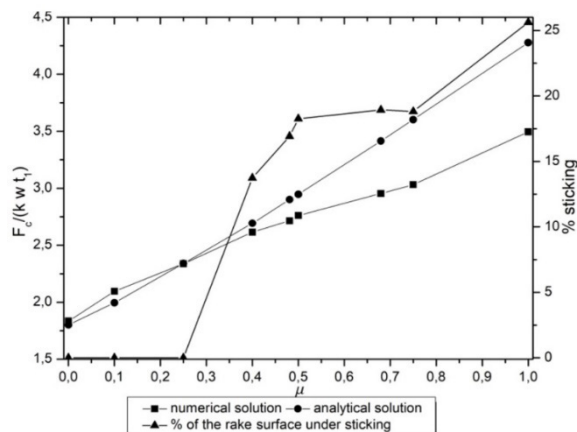**Figure 19** Non-dimensional cutting forces and friction coeffi-cient for rake angle α = 0o.

Figure 20 Non-dimensional cutting forces and friction coeffi-cient for rake angle α = 6o.

In the Figures 19 and 20, the numerical and the analytical cutting forces stated from Equations (3) and (4) found in Molinari and Moufki (2008) are compared. There is a convergence between both solutions when only sliding occurs (% sticking=0). As sticking occurs, there is a divergence between the solutions. This divergence is due to the fact that analytical solutions do not predict the formation of the sticking region. While the analytical cutting forces increases linearly with friction coefficient μ, the numerical solution increases at a lower rate because. Similarly to the results observed in Table 4, with the occurrence of sticking, the apparent friction coefficient is lower than the sliding friction coefficient, resulting in smaller cutting forces.

The influence of the advancement of sticking regions on the rake surface with the cutting forces can be observed when considering a restricted contact tool, where the contact length l/t_1 is fixed, and varying the friction coefficient at the chip-tool interface. The following figure shows a graph of the cutting forces against the friction coefficient at the contact interface, with $l/t_1 = 1/\cos(\alpha)$ and $\alpha = 6°$:
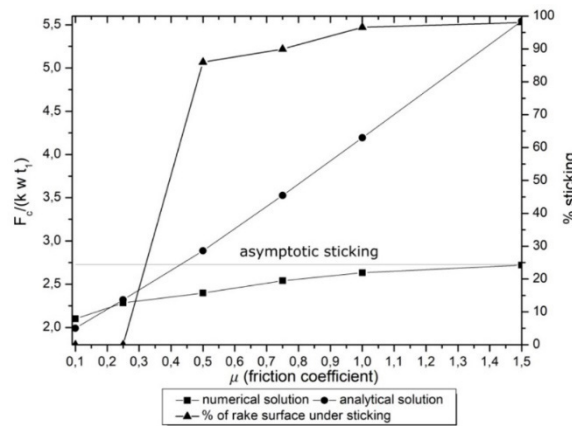
Figure 21 Cutting forces x friction coefficient for a restricted contact tool.

Figure 21 shows an increase in the sticking regions on the contact surface with the friction coefficient. In cases where sticking prevails ($\mu \geq 0.5$), the numerical cutting forces become independent of the friction coefficient, converging towards an asymptotic value while the analytical solution increases linearly. The asymptotic value constitute an upper bound for cutting forces, obtained by enforcing tangential restriction across the entire contact region (100% sticking).

This independence of cutting forces from the friction coefficient between the chip and the tool can be observed through comparison with the apparent friction coefficient, determined by the ratio of shear to normal stresses at the contact. The following table presents this comparison:

Table 4 Tool-chip and apparent friction coefficients

μ	0.10	0.25	0.50	0.75	1.0	1.5
μ_{app}	0.1206	0.2657	0.3169	0.2968	0.3106	0.2592

In Table 4, when there is only sliding (cases $\mu = 0.10$ and $\mu = 0.25$), the obtained apparent friction coefficient approaches the friction coefficient between the chip and the tool. The difference between them is justified by the nature of the numerical solution. For cases where sticking prevails, the apparent friction coefficient is always lower than the friction coefficient between the chip and the tool.

Regarding the shear angle, the work by Molinari and Moufki (2008) demonstrates that after chip formation, the shear angle ϕ^* can be distinct from the angle ϕ_M estimated by Merchant without considering chip formation. Despite predicting this behavior, the optimal angle ϕ^* is not calculated analytically.

Below, the optimum shear angles obtained numerically are presented, considering the rake angles $\alpha = 0°$ and $\alpha = 6°$, along with the angles predicted by Merchant's model, determined by Equation (14):
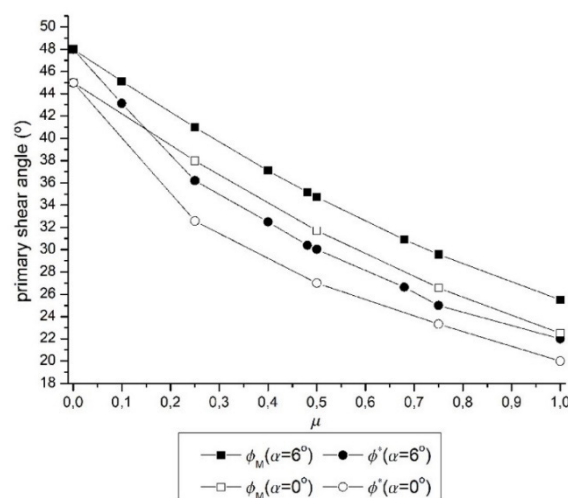

Figure 22 Primary shear angles and friction coefficient.

According to Figure 22, the primary optimal shear angles ϕ^* and those predicted by Merchant (ϕ_M) agree only in the frictionless case, $\mu = 0$. The primary shear region, besides depending on the tool rake angle α and the friction angle β, also depends on the contact length of the chip-tool contact and the sticking/sliding regimes, which can also change its angle and shape, as shown in the following figures:
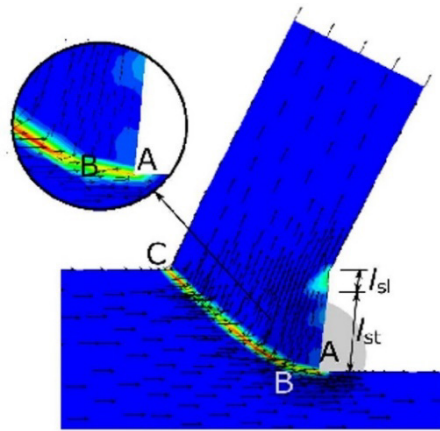

Figure 23 Primary shear zone and velocity filed for α = 6o, μ = 0.50, l/t1 = 1.0055.

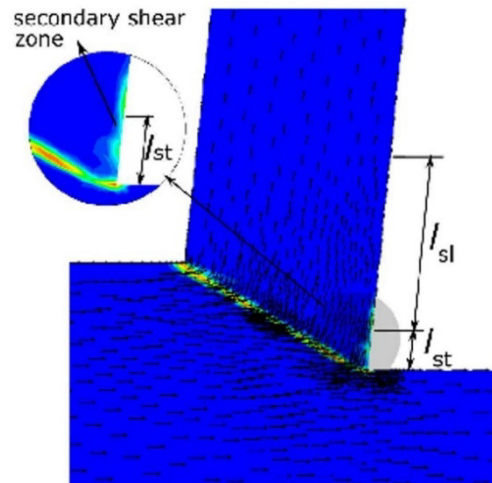**Figure 24** Primary shear zone and velocity filed for α = 6o, μ = 0.50, l/t1 = 2.0.

In Figure 23, which represents the situation of a tool with restricted contact, sticking prevails ($l_{st}/l = 0.86$) on the tool rake face, while sliding occurs in a smaller length ($l_{sl}/l = 0.14$). Due to material sticking, an additional shearing mechanism is observed alongside the shear zone AB, constituting the tertiary shear zone along. The plastic deformations (rates) occurring in region AB are due to the sliding between adjacent planes, between the plane of the stationary material ahead of the tool rake face and above AB and the portion of material flowing under the tool. This tertiary region is not responsible for chip formation as in BC, and due to the presence of this stationary material, it can lead to the formation of a built-up Edge (BUE).

On the other hand, Figure 24 illustrates the scenario where the sliding region predominates over the sticking one ($l_{sl}/l = 0.82$ and $l_{st}/l = 0.18$, respectively). In this situation, the primary shear zone remains straight, and a secondary shear zone is formed. The chip material flows over the portion of the contact under sticking along lst, resulting in plastic deformations (rates) and sliding with friction along l_{sl}. Consequently, the chip flows with a low curvature and almost parallel to the tool rake face.

4 CONCLUSIONS

This work presented a limit analysis approach for examining the orthogonal cutting process. In the proposed formulation, the friction dissipation term is considered and the contact problem is solved, enabling the determination of tangential velocities and stresses at the contact as parts of the solution. This contribution allows the delineation of regions

of sticking and sliding at the tool-chip interface. It stands apart from conventional methods found in the literature, such as those discussed in Santos et al. (2023), which presuppose the extensions of these sliding/sticking regions.

Also, as a contribution, this approach enables the simultaneous and independent verification of stress plasticity admissibility conditions (restriction (11)) and Coulomb's friction law in the contact region (restriction (12)). This demonstrates that whether sticking or sliding is present, points of plasticization can occur within the contact area, as illustrated in Figures 12 and 13, along with the corresponding extensions of sticking and sliding depicted in Figures 14 and 15. Plasticization manifests across nearly the entire contact length l. Unlike approaches encountered in the literature, it is emphasized that the plasticization condition hinges on combination between normal and shear stresses. Imposing conditions directly on shear stress, as found in literature, it may yield inconsistencies since pure shear stress is not observed within the contact region.

As a preliminary stage, the methodology underwent validation through a comparative analysis of numerical and experimental findings in Abouridouane et al. (2015). In the numerical approach, since the contact length is not known a priori, it was gradually increased from $l = t_1/ \cos(\alpha)$ until the normal contact stress approached zero at the point of separation. Examination of Table 2 reveals a close proximity between the experimental contact lengths lexp and the numerical ones lnum, underscoring the predictive efficacy of the implemented contact problem. Regarding the cutting forces, the differences between the experimental and numerical results were 5% and 12.1%, respectively. Despite disregarding viscous and temperature effects, which can lead to material stiffening or softening, the elastic and perfectly-plastic model used in limit analysis provides a good estimation for the cutting forces. Regarding the experiments, one should consider potential uncertainties in measurements, tool positioning, material properties, and other sources that may introduce errors.

After this stage, a more comprehensive numerical study was conducted, considering tools with rake angles of $\alpha = 0º$ and $\alpha = 6º$. In Figure 18, it is observed the dependence of contact lengths with the tool rake angles and the friction coefficient at the tool-chip interface. For a smaller rake angle ($\alpha = 0º$), the contact lengths are greater than for those ones for ($\alpha = 6º$) because the tool acts more strongly as a barrier. The numerical results presented were compared with various expressions found in Fatima and Mativenga (2013) and presented a good agreement with the analytical models proposed by Hahn-Rubenstein-Zorev. However, there is no consensus on the factor m, which is regarded by some authors as a factor depending on the stress distribution in the secondary region, a factor of ignorance, or a parameter varying between 5 and 22. In this numerical study, a factor $m = 1.10$ closely approximates the theoretical curve with the numerical results obtained.

Regarding the cutting forces shown in Figures 19 and 20, the numerical and analytical forces are compared and related with sticking and sliding occurrence in the contact region. While numerical and analytical cutting forces are near when sliding occur (sticking = 0%), they diverge with the advancement of the region under sticking. This divergence is linked to the difference between the apparent friction coefficient μapp, determined by the ratio between the shear and normal stresses at the contact, and the friction coefficient μ between the chip and the tool in sliding, as similarly observed in Table 3. Part of chip slides over the adhered material with μapp < μ and other part slides along the rake face with friction coefficient μ.

This behavior of the cutting force with the occurrence of sticking becomes more evident in a case of restricted contact tool when fixing the contact length l and varying the friction coefficient μ. As long as friction coefficient increases, sticking becomes predominant and the cutting forces tend towards an asymptotic value, determined by imposing tangential restrictions throughout the contact. For higher friction coefficients, the cutting forces become independent of the sliding friction coefficient μ, with $\mu_{app} < \mu$ as presented in Table 4. The cutting forces are lower-limited by the frictionless case and upper-limited by the occurrence of complete sticking.

This study also confirms the proposition outlined in the work of Molinari and Moufki (2008) regarding the shear angle, elucidating that when chip formation is taken into account, there exists a distinction between the shear angles (ϕ_M) and ϕ^*. The theoretically predicted optimal angles ϕ^* from Molinari and Moufki (2008) were numerically numerically obtained, as illustrated in Figure 22. Notably, it is observed that the angles (ϕ_M) and ϕ^* converge solely when $\mu = 0$. Although chip formation is considered in these numerical simulation (for $\alpha = 0º$ and $\alpha = 6º$), the contact lengths are on the order of the ratio $l = t_1/ \cos(\alpha)$, as shown in Figure 18, approaching the case used for the deduction of the primary angle in Figure 2.

Author's Contribuitions: Conceptualization, FF Figueiredo, L Borges, JL Silveira; Methodology, FF Figueiredo, L Borges; Investigation, FF Figueiredo, L Gomes; Writing - original draft, FF Figueiredo; Writing - review & editing, L Borges, JL Silveira and L Gomes; Resources, L Borges and JL Silveira; Supervision, FF Figueiredo.

Editor: Marco L. Bittencourt

References

Abouridouane, M., Klocke, F., Lung, D., and Veselovac, D. (2015). The mechanics of cutting: In-situ measurement and modelling. 15th CIRP Conference on Modelling of Machining Operations, 31:146–251.

Afsharhanaei, A., Rebaioli, L., Parenti, P., and Annoni, M. (2016). Finite element modeling of micro-orthogonal cutting process with dead metal cap. Journal of Engineering Manufacture, pages 1–11.

Armarego, E. J. A. and Brown, R. H. (1969). The Machining of Metals. Prentice-Hall, New Jersey.

Borges, L., Zouain, N. Costa, C., and Feijoo, R. (2001). An adaptive approach to limit analysis. International Journal of Solids and Structures, 38:1707– 1720.

Borges, L. A., Zouain, N., and Huespe, A. E. (1996). A nonlinear optimisation procedure for limit analysis. European Journal of Mechanics /A Solids, 15:487–512.

Cai, L., Feng, Y., and Liang, S. (2024). Analytical modelling of cutting force in end-milling with minimum quantity lubrication. International Journal of Precision Engineering and Manufacturing.

Chabrand, P., Dubois, F., and Raous, M. (1998). Various numerical methods for solving unilateral contact problems with friction. Mathematical and Computer Modelling, 28:97–108.

Chen, W. F. and Liu, X. L. (1990). Limit Analysis in Soil Mechanics. Elsevier Science Publishing, Amsterdam.

Denguir, L., Outeiro, J. C., Rech, J., Frometin, G., Vignal, V., and Besnard, R. (2017). Friction model for tool/work material contact applied to sur- face integrity prediction in orthogonal cutting simulation. Procedia CIRP, 58:578–583.

DeVries, W. R. (1992). Analysis of Material Removal Process. Springer-Verlag, USA.

Fatima, A. and Mativenga, P. (2013). A review of tool-chip contact length models in machining and future direction for improvement. Proceedings of the Institution of Mechanical Engineers Part B, 227:345–356.

Figueiredo, F. and Borges, L. (2017). Limit analysis formulation for frictional problems. Archive of Applied Mechanics, 86:1965–1977.

Figueiredo, F. and Borges, L. (2020). Limit analysis and frictional contact: formulation and numerical solution. Meccanica, 55:1347–1363.

Groover, M. (2010). Fundamentals of Modern Manufacturing. John Willey Sons, USA.

Grzesik, W. (2008). Advanced Machining Processes of Metallic Materials: Theory, Modelling and Applications. Elsevier.

Grzesik, W. (2017). Advanced Machining Processes of Metallic Materials. Elsevier, Amsterdam, Netherlands.

Kalpakjian, S. and Schmid, S. R. (2016). Manufacturing Processes for Engineering Materials. Pearson.

Kovrizhnykh, A. M. (2009). Determining the shear angle, forces, and sizes of shearing elements during metal cutting. Journal of Applied Mechanics and Technical Physics, 50:147–154.

Kudo, H. (1965). Some slip-line solutions for two-dimensional steady-state machining. International Journal of Mechanical Sciences, 7:43–55.

Lubliner, J. (1990). Plasticity Theory. Pearson Education, USA.

Medina-Clavijo, B., Sela, A., Arrieta, I. M., Fedorets, A., Arrazola, P. J., and Chuvilin, A. (2021). In-sem micro-machining reveals the origins of the size effect in the cutting energy. Scientific Reports, 11.

Michalowski, R. and Mroz, Z. (1978). Associated and non-associated sliding rules in contact friction problems. Archives of Mechanics, 30:259–276.

Molinari, A., Cheriguene, R., and Miguelez, H. (2011). Numerical and analytical modeling of orthogonal cutting: The link between local variables and global contact characteristics. International Journal of Mechanical Sciences, 53:183–206.

Molinari, A. and Moufki, A. (2008). The merchant's model for orthogonal cutting revisited: A new insight into the modeling of chip formation. International Journal of Mechanical Sciences, 50:124–131.

Nguyen, Q. S. (2000). Stability and Nonlinear Solid Mechanics. John Wiley Sons, England.

Ozlu, E., Molinari, A., and Budak, E. (2010). Two-zone analytical contact model applied to orthogonal cutting. Machining Science and Technology, 14:323–343.

Peter, M., Sauer, K., Regel, J., and Dix, M. (2022). Effects of orthogonal cutting with different cutting edge microgeometry on the surface integrity of unidirectional carbon fiber reinforced plastics. Proceedings of 22nd Machining Innovations Conference for Aerospatial Industry, pages 80–87.

Raous, M. (1999). Quasistatic signorini problem with coulomb friction and coupling to adhesion. CISM Courses and Lectures: New Developments in Problems, 384:101–178.

Santos, A., Bonfim, M., Silva, L., Silva, R. B., Camara, M. A., Magalhães, F. C., and Abrão, A. M. (2023). Determination of the chip–tool contact length in orthogonal cutting. Journal of Tribology, 145.

Sauer, K., Witt, M., and Putz, M. (2019). Influence of cutting edge radius on process forces in orthogonal machining of carbon fiber reinforced plastics (cfrp). Procedia CIRP, 85:218–223.

Saxcé, G. and Bousshine, L. (1998). Limit analysis theorems for implicit standard materials: Application to the unilateral contact with dry friction and the non-associated flow rules in soils and rocks. International Journal of Mechanical Science, 40:387–398.

Strenkowski, J. S. and Moon, K. J. (1990). Finite element prediction of the chip geometry and tool/workpiece temperature distributions in orthogonal metal cutting. Journal of Engineering for Industry, 112:313–318.

Tyan, T. and Yang, W. H. (1992). Analysis of orthogonal metal cutting process. International Journal for Numerical Methods in Engineering, 34:365–389.

Wojciechowski, S., Matuszak, M., Powalka, B., Madajewski, M., Maruda, R., and Królczyk, G. (2019). Prediction of cutting forces during micro end milling considering chip thickness accumulation. International Journal of Machine Tools and Manufacture, 147:103466.

Wriggers, P. (1999). Finite elements for thermomechanical contact and adaptive finite element analysis of contact problems. CISM Courses and Lectures: New Developments in Contact Problems, 384:177–246.

Wu, M., Zhang, G., Wang, T., and Wang, R. (2023). Milling force modeling methods for slot milling cutters. Machines, 11:922.

Zhang, C., Lu, J., Zhang, F., and Butt, S. I. (2017). Identification of a new friction model at tool-chip interface in dry orthogonal cutting. International journal of Advanced Manufacturing Technology, 89:921–932.

Zhou, J. and Ren, J. (2020). Predicting cutting force with unequal division parallel-sided shear zone model for orthogonal cutting. International Journal of Advanced Manufacturing Technology, 107:4201–4211.